International Journal of Fluid Machinery and Systems
Vol. 4, No. 4, October-December 2011

DOI: http://dx.doi.org/10.5293/IJFMS.2011.4.4.375
ISSN (Online): 1882-9554

**Original Paper**

# Computational Study of the Magnetically Suspended Centrifugal Blood Pump (2nd Report: Pressure Fluctuation and Stability of Impeller Rotation for Different Volute Shapes)

**Yoshifumi Ogami[1], Daisuke Matsuoka[2] and Masaaki Horie[3]**

[1]Department of Mechanical Engineering, Ritsumeikan University
1-1-1 Noji-Higashi, Kusatsu 525-8577, Japan, y_ogami@cfd.ritsumei.ac.jp
[2]Department of Mechanical Engineering, Ritsumeikan University, daisuke_matsuoka@ntn.co.jp
[3]Department of Mechanical Engineering, Setsunan University
17-8 Ikedanakamachi, Neyagawa, Osaka 572-8508, Japan, m-horie@mec.setsunan.ac.jp

**Abstract**

The turbo-type blood pump studied in this paper has an impeller that is magnetically suspended in a double volute casing. The impeller rotates with minimal fluctuations caused by fluid and magnetic forces. In order to improve stability of the rotating impeller and to facilitate long-term use, a careful investigation of the pressure fluctuations and of the fluid force acting on the impeller is necessary. For this purpose, two models of the pump with different volute cross-sectional area are designed and studied with computational fluid dynamics software. The results show that the fluid force varies with the flow rate and shape of the volute, that the fluctuations of fluid force decrease with increasing flow rate and that the vibratory movement of the impeller is more efficiently suppressed in a narrow volute.

***Keywords:*** Computational Fluid Dynamics, Centrifugal Blood Pump, Pressure Fluctuation, Stability of Impeller Rotation, Numerical Analysis

## 1. Introduction

The drawback of pulsatile displacement-type blood pumps is that, compared to turbo-type blood pumps, they contain more components and are considerably larger and more expensive. On the other hand, the drawbacks of turbo-type blood pumps are (1) that the shaft seal in the casing is a potential source of blood leakage and of contamination by foreign matter, and (2) that frictional heat produced at the seal promotes the formation of clot and causes the destruction of red blood cells. As a result, turbo-type blood pumps can only be used for short periods of time, despite their advantage over pulsatile displacement-type pumps (Akamatsu [1]).

To overcome the shortcomings of turbo-type blood pumps and to allow their use over longer time periods, Akamatsu et al. have designed a magnetically suspended centrifugal blood pump in such a way that the impeller rotates in the bloodstream without making any contact with the casing as a result of the interaction between the permanent magnet and the electromagnet (Akamatsu et al. [2]-[5]). Further, the stability of the rotating impeller is improved by using straight radial blades and a double volute casing (Akamatsu [3]).

In order to suspend the rotating impeller with the magnetic force, rotations about all axes are actively controlled by the system. The impeller is located at the center of the coordinate system and its axis is labeled as the $z$-axis. However, translational movements of the impeller along $x$- and $y$-axes are controlled passively by the magnetic force produced by the magnet implanted in the impeller. Therefore, motion along the z-axis is neither stable nor well constrained (Akamatsu [3], Tsukiya et al. [5]). Although the stability is improved by the design mentioned above, the asymmetry of the fluid force distribution and the magnetic force distribution acting on the rotating impeller cause the axis of the impeller to undergo small-amplitude vibratory motion. If this amplitude is not small enough, the rate of hemolysis and power consumption of the system increase. Furthermore, the impeller may collide with the wall of the diffuser, resulting in a loss of control.

It is therefore important to clarify the mechanism of the vibration of the impeller axis in order to avoid these potential

Received March 25 2011; revised June 14 2011; accepted for publication November 28 2011: Review conducted by Prof. Tong-Seop Kim. (Paper number O11005K)
Corresponding author: Yoshifumi Ogami, Professor, y_ogami@cfd.ritsumei.ac.jp

problems and to make the blood pump system more efficient in terms of size, weight, and energy consumption. However, analyzing the fluid and magnetic forces acting on the impeller and their interaction is a complex task. As a first step in that direction, we focus on the fluid force only and perform a detailed analysis with a simulation. Using two design models for the casing with different volute cross-sectional areas, we investigate the pressure fluctuations in the pump as well as the fluid force acting on the impeller. It is difficult to simulate the vibratory movement of the impeller's axis and create an appropriate computational grid for this movement at every time step; therefore, the simulation assumes a fixed impeller axis. Our pump differs markedly from a usual turbo pump in that its specific speed is about 100 and the machine Reynolds number is about 50,000. Moreover, the diameters of the inlet and outlet are about 10 mm, the impeller is suspended and rotates by the magnetic force, and the volute casing has two layers. By studing this pump, we find that the average pressure distributions for the two models are almost symmetrical with respect to the center of the impeller while the pressure fluctuations are somewhat scattered, that the fluctuation amplitude of fluid force decreases with increasing flow rate, and most importantly that the vibration of the impeller is more efficiently suppressed for the narrower volute.

## 2. Computational Model and Method

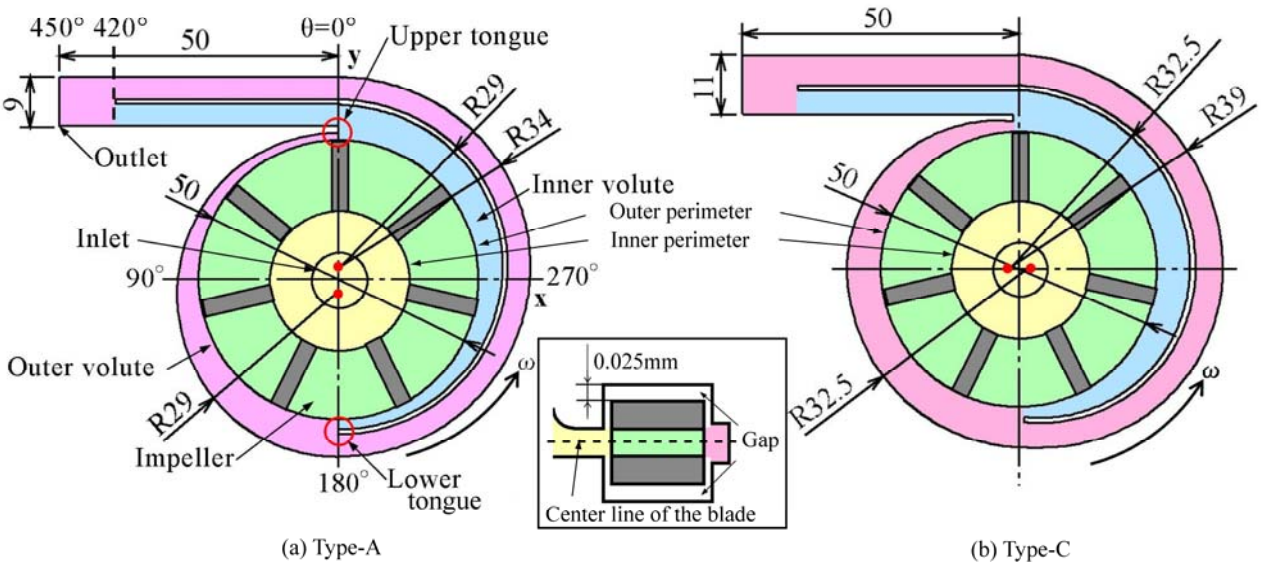


**Fig. 1** Computational models

Our pump is designed to be used as an implantable cardiac assistive blood pump, which requires a diameter of the pump inlet and outlet of about 10 mm. This takes into account the relationship with the aorta and a cannula used for implanting the device. Further, the double volute casing makes it difficult to increase the volute cross-sectional area at the outlet, as is usually done. For this reason, we have designed two computational models, Type-A and Type-C, illustrated in Fig.1. Type-A has the centers of the outer and inner volutes displaced by $\pm 2.5$ mm in the $y$-direction and Type-C has them displaced by $\pm 1.5$ mm in the $x$-direction, as shown by the red dots in the figure. The model referred to as Type-B was used in [6]. Both types comprise an inlet (the portion painted yellow), an impeller (green), a volute (blue and pink), and a gap of 0.025 mm (see inset). The straight radial blades of the impeller have the following specifications: number of blades $Z_1 = 7$, blade height $b = 3.5$ mm, internal radius $r_1 = 13$ mm, and external radius $r_2 = 25$ mm. In both types, the outer volute (pink) extends from the upper tongue at $\theta = 0^\circ$ to a short distance before the outlet at $\theta = 420^\circ$ and leads to the outlet at $\theta = 450^\circ$. (Angles greater than $360^\circ$ are used for convenience.) The inner volute (blue) extends from $\theta = 180^\circ$ to $\theta = 420^\circ$.

Figure 2 shows the cross-sectional areas of the inner and outer volutes, and their total values as functions of $\theta$ for both models. The area of the outer volute between $0^\circ$ and $180^\circ$ is the same as that of the inner volute between $180^\circ$ and $360^\circ$ in both cases, but the total area for Type-A is smaller than for Type-C at all angles except at the outlet ($\theta = 450^\circ$).

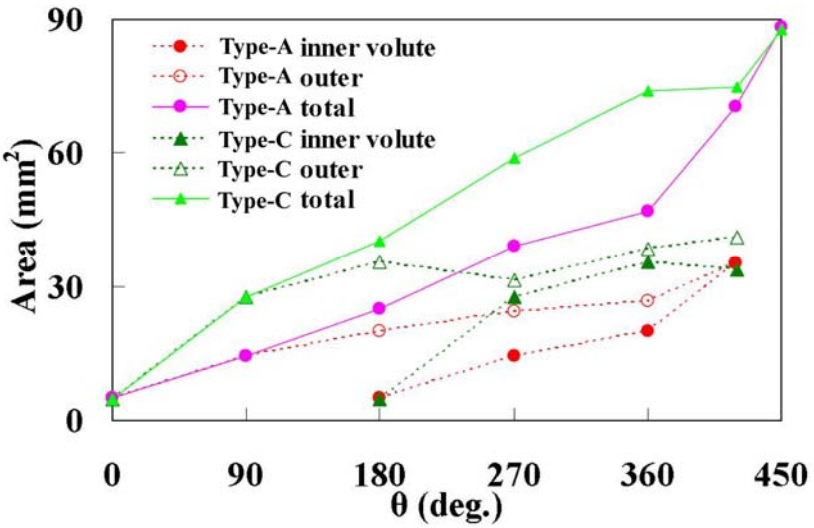


**Fig. 2** Cross-sectional area

To simulate fluid flow in the pump, and calculate the velocity, the pressure, and the fluid force, we use a general-purpose thermal fluid analysis software, "FLUENT" (produced by ANSYS, Inc.) already used in our previous study [6]. Table 1 shows the number of grid points for each part separately and the total number for the two model types. The numbers differ for the volute and the gap because the volutes have a different shape. However, the total numbers are almost the same.

The rotation speed of the impeller is set to $n$ = 2,000 rpm. The other conditions for the simulations are the same as those used in [6]. Average values and standard deviations are calculated over five rotations, when the flow in the pump is considered to have reached a quasi-steady state. The distributions of physical values such as the velocity and the pressure in the $x$-$y$ plane, i.e., perpendicular to the impeller axis and passing through the center of the blades (see the middle figure in Fig.1), are also plotted.

**Table 1** Number of grid points used for each part of the two models

| | Inlet | Impeller | Volute | Gap | Total |
|---|---|---|---|---|---|
| Type-A | 27,829 | 23,625 | 65,808 | 116,922 | 234,184 |
| Type-C | 27,829 | 23,625 | 73,120 | 115,482 | 240,056 |

## 3. Pump characteristics

Figure 3 shows the simulation results for the pump characteristics at the outlet, i.e., the non-dimensional flow rate, $\phi$, and the non-dimensional pressure, $\psi$, resulting essentially from the motion of the impeller blades. Note that the normal adult flow rate, $Q \approx 5.0$ L/min, corresponds approximately to $\phi$ =0.03, and the blood pressure, $P \approx 120$ mmHg, approximately to $\psi$ = 0.55. The outlet pressure for Type-A is larger than for Type-C over the range $\phi$ = 0 to 0.044, and the outlet pressure for Type-C exceeds that for Type-A at $\phi$ =0.044. These results suggest that Type-A, which produces higher pressures, is suitable for patients who require these higher blood pressures, and that Type-C, which produces higher pressures at large flow rate, is suitable for larger patients who need a large blood flow rate.

Details of the fluid flow characteristics are described in the next section.

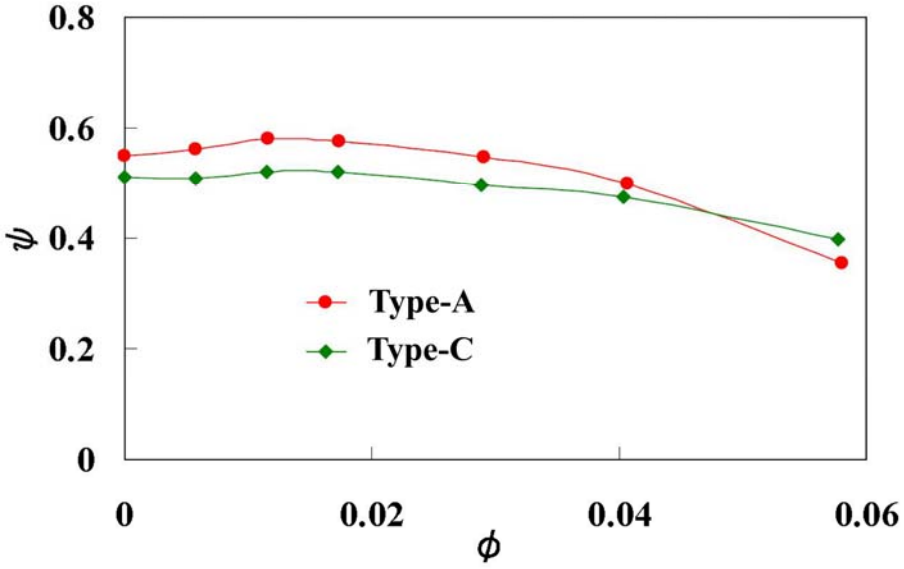


**Fig. 3** Flow rate and generated pressure

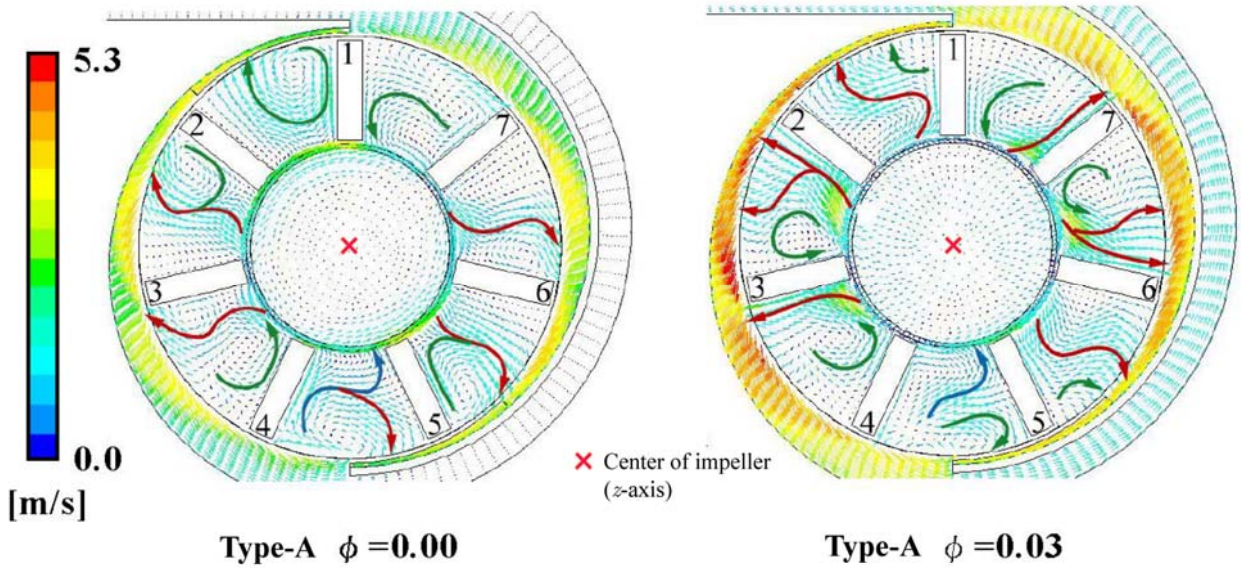


**Fig. 4** Relative velocity vectors (small arrows) and stream lines (large arrows)

## 4. Flow inside the pump

Figure 4 shows the instantaneous relative velocity vectors (small arrows) inside the Type-A impeller for $\phi$ = 0.00 and 0.03. The large arrows represent the stream lines. The seven blades are numbered counterclockwise with the blade closest to the upper tongue labeled 1. The flow in the direction from the center of impeller (marked as ×) to the outer circumference of the impeller is referred to as forward current, and the flow in the opposite direction is referred to as the backward current. Whereas, in a traditional pump, only the forward current is observed everywhere between the blades, our pump also displays additional flow patterns between the blades, such as backward current and vortex flow. The reason for this may be that the flow path is broader than necessary, as the blade height $b$ = 3.5mm is much larger than in the traditional design (less than 1 mm), and the inlet and outlet angles of the blades are 90°.

The flow patterns in Type-C are qualitatively the same as in Type-A.

The flow rate between each impeller blade and the total flow rate $\phi_l$ for $\phi$ = 0.00 and 0.03 are listed in Table 2. These values are the mean flow rates between each pair of blades during one pitch of rotation from the position shown in Fig. 4, while $\phi_l$ is the total flow rate along the impeller's outer perimeter. Positive values indicate a forward current, and negative values a backward current. Note that the total flow rate $\phi_l$ exceeds the outlet flow $\phi$ because the flow traversing the gap from the volute to the inlet (leakage flow) re-enters the impeller [6].

**Table 2** Flow rate at each section

| section | $\phi = 0.00$ | | $\phi = 0.03$ | |
|---|---|---|---|---|
| | Type-A | Type-C | Type-A | Type-C |
| 1-3 | $5.9\times10^{-3}$ | $6.3\times10^{-3}$ | $9.2\times10^{-3}$ | $11.7\times10^{-3}$ |
| 2-4 | $5.2\times10^{-3}$ | $2.3\times10^{-3}$ | $9.4\times10^{-3}$ | $4.7\times10^{-3}$ |
| 3-5 | $-3.1\times10^{-3}$ | $-2.4\times10^{-3}$ | $0.2\times10^{-3}$ | $-0.1\times10^{-3}$ |
| 4-6 | $1.3\times10^{-3}$ | $3.5\times10^{-3}$ | $2.9\times10^{-3}$ | $6.3\times10^{-3}$ |
| 5-7 | $7.0\times10^{-3}$ | $5.2\times10^{-3}$ | $10.5\times10^{-3}$ | $9.0\times10^{-3}$ |
| 6-1 | $1.0\times10^{-3}$ | $-0.1\times10^{-3}$ | $7.1\times10^{-3}$ | $4.6\times10^{-3}$ |
| 7-2 | $-3.9\times10^{-3}$ | $-1.1\times10^{-3}$ | $1.9\times10^{-3}$ | $4.8\times10^{-3}$ |
| $\phi_I$ | 0.0134 | 0.0137 | 0.0412 | 0.0410 |

In the case of $\phi = 0.00$, a forward current is created soon after the blade passes near the upper tongue (sections 1-3 and 2-4 in Table 2) and a backward current emerges when the blade passes near the lower tongue, as indicated by a negative value for section 3-5. Sections 4-6 and 7-2, which are nearly symmetrically located relative to sections 1-3 and 3-5, show a similar tendency. As for Type-C at $\phi = 0.00$, because the cross section at the beginning of the volute is larger than in Type-A, the forward current in section 1-3 is larger. This current decreases to less than half (section 2-4) and a backward current merges at section 3-5. In the case of $\phi = 0.03$, a large forward current is created for both Type-A and Type C after the blade passes near the upper tongue, and the current becomes very small in section 3-5.

For both $\phi = 0.00$ and 0.03, the forward current in Type-C is larger than in Type-A at section 1-3. The total currents in sections 1-3, 2-4, and 3-5 for Type-A are larger than those for Type-C. This indicates that a larger backward current is created for Type-C as the blade approaches the lower tongue. This backward current or vortex flow causes a pressure drop, which results in a lower outlet pressure for Type-C, as shown in Fig. 3 for $\phi$<0.044.

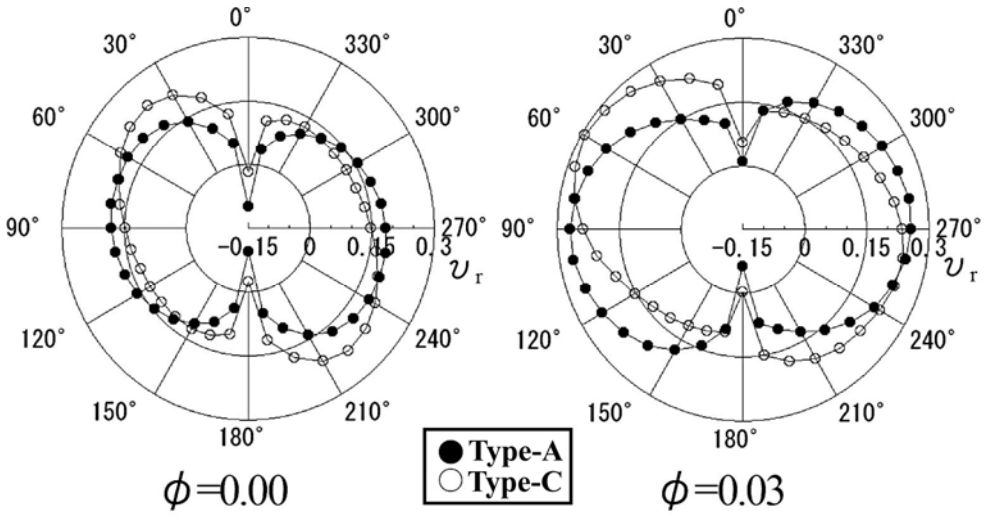


**Fig. 5** Radial velocity along the outer impeller perimeter

Figure 5 shows the averaged radial velocity $v_r$ on the outer impeller perimeter, at a distance of 25.5 mm from the center of the impeller. The velocity is measured at points separated by an angle of $10^\circ$. We observe a backward current near both the upper and lower tongues for both models at $\phi = 0.00$, whereas a backward current appears only for Type-A near the lower tongue at $\phi = 0.03$.

## 5. **Pressure on the outer circumference of impeller**

Stable rotation of the impeller is important, especially because it is magnetically suspended and rotates without a shaft so that rigidity to a lateral load is not very high. This section examines the pump stability by considering the pressure on the outer impeller perimeter. The next section considers the pressure inside the volute.

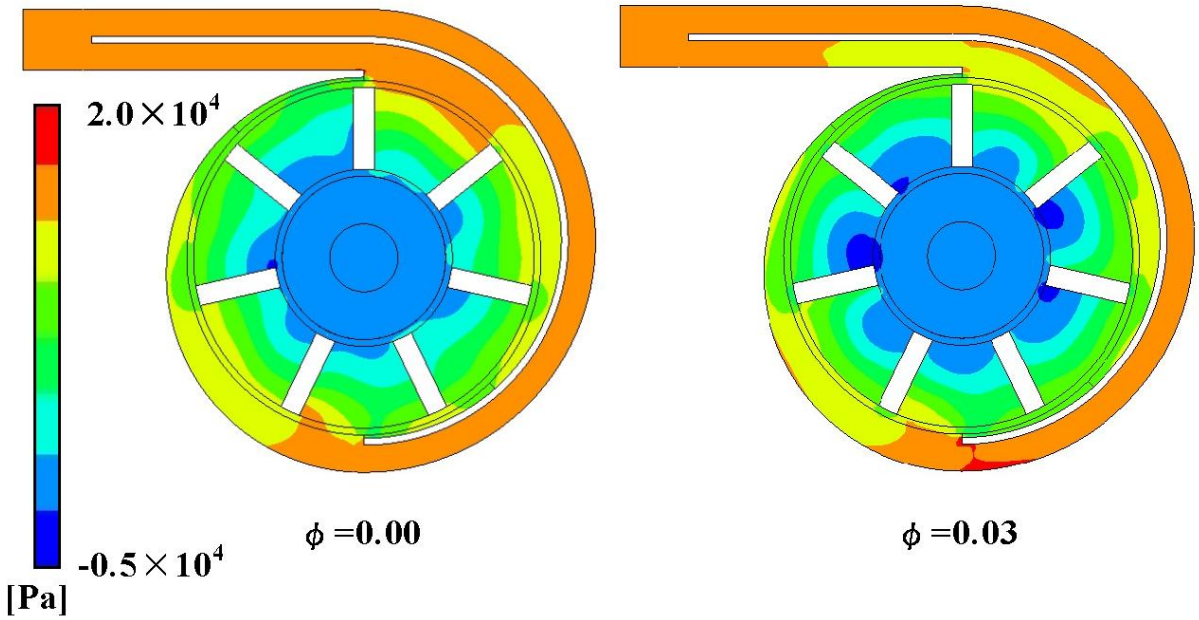


**Fig. 6** Pressure distribution for the Type-A model

Figure 6 shows the entire pressure distributions for the Type-A model at $\phi = 0.00$ and 0.03. There is no flow out of the outlet when $\phi = 0.00$ , which results in a larger overall pressure than when $\phi = 0.03$. The total flow rate from the outer perimeter at $\phi = 0.00$ is small but non-zero (Table 2) because of the leakage through the gap. There is no forward current along the front of the blade (Fig.4), and the pressure difference between the front and back of each blade is small.

In the case of $\phi = 0.03$, a forward current is generated along the front of the blade and the pressure difference between the front and the back is larger than when $\phi = 0.00$. The Type-C model gives a very similar result.

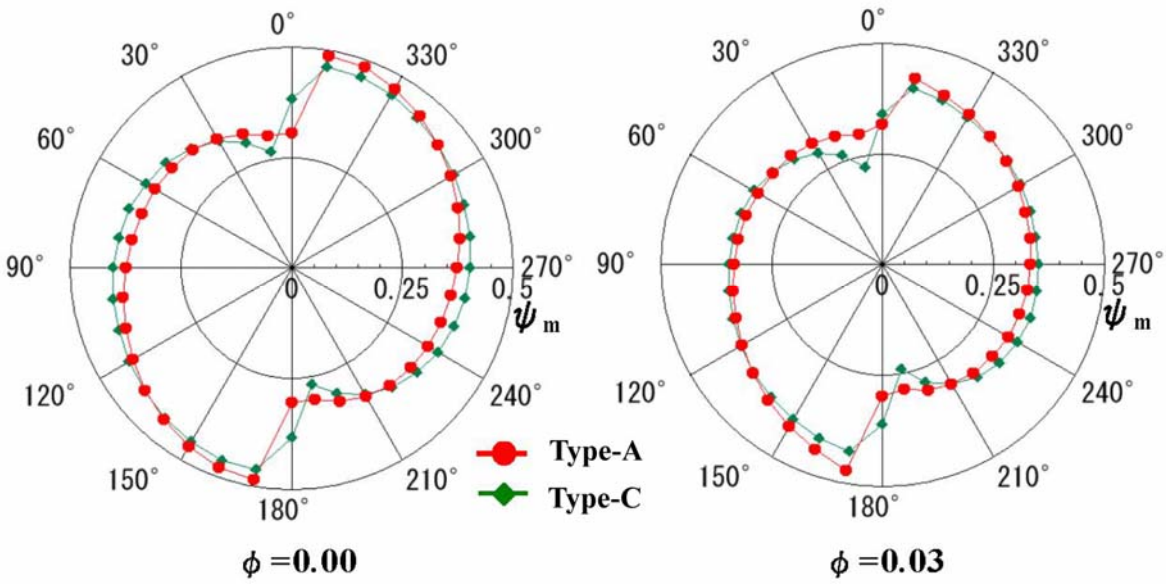


**Fig. 7** Non-dimensional averaged pressure along the outer perimeter

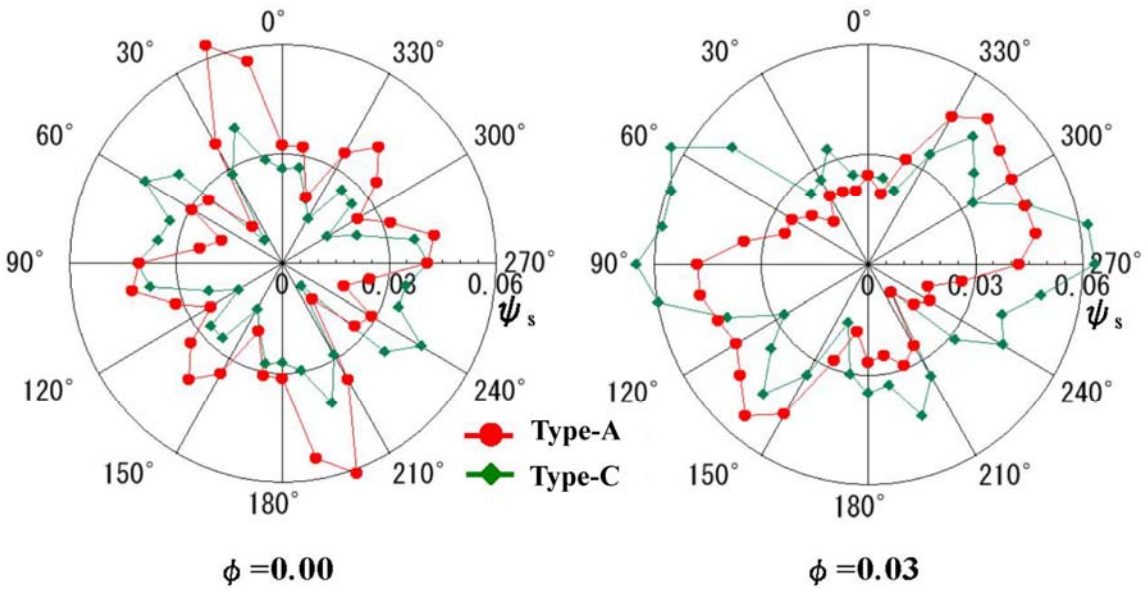


**Fig. 8** Standard deviation of the non-dimensional pressure along the outer perimeter

The non-dimensional pressure distributions $\psi_m$ along the outer perimeter of the impeller at $\phi = 0.00$ and 0.03 are shown in Fig. 7, and the standard deviation of the non-dimensional pressure $\psi_s$ in Fig. 8. The pressure is measured at the same locations as in Fig. 5. Regardless of the flow rate, Fig. 7 shows that the pressure increases from the upper and lower tongues with increasing angle for both model types. For $\phi = 0.00$, the average pressures for both models are almost the same and, due to the symmetric design of the double volute casing with respect to the impeller center, the pressure distributions are also symmetrical. For $\phi = 0.03$, the average pressure on the outer perimeter decreases due to a decrease in the overall pressure inside the pump. The pressure distributions are almost symmetrical with respect to the center for the same reason. The pressure between $90^\circ$ and $170^\circ$ in the outer volute is slightly greater than between $270^\circ$ and $350^\circ$ in the inner volute because the length of the outer volute from the upper tongue to the outlet is larger than the length of the inner volute from the lower tongue to the outlet. Therefore, more fluid resistance has to be overcome. The pressure in Type-A between $10^\circ$ and $30^\circ$ is higher than in Type-C because of the narrower channel of Type-A near the upper tongue.

The standard deviation, shown in Fig. 8, for Type-A at $\phi = 0.00$ between $0^\circ$ and $30^\circ$, and between $180^\circ$ and $210^\circ$ is larger than in other regions. This is because the overall pressure is high due to the zero flow rate, and a sudden increase or decrease in the pressure occurs periodically as the blades pass near the upper and lower tongues, where the channel is very narrow. For $\phi = 0.03$, the standard deviations in Type-A in the ranges $90^\circ$-$150^\circ$ and $270^\circ$-$330^\circ$, and in Type-C in the ranges $50^\circ$-$140^\circ$ and $240^\circ$-$320^\circ$, are larger because the flow pattern varies drastically from a forward current on the front of the blade to a backward current or vortex flow on the back of the blade.

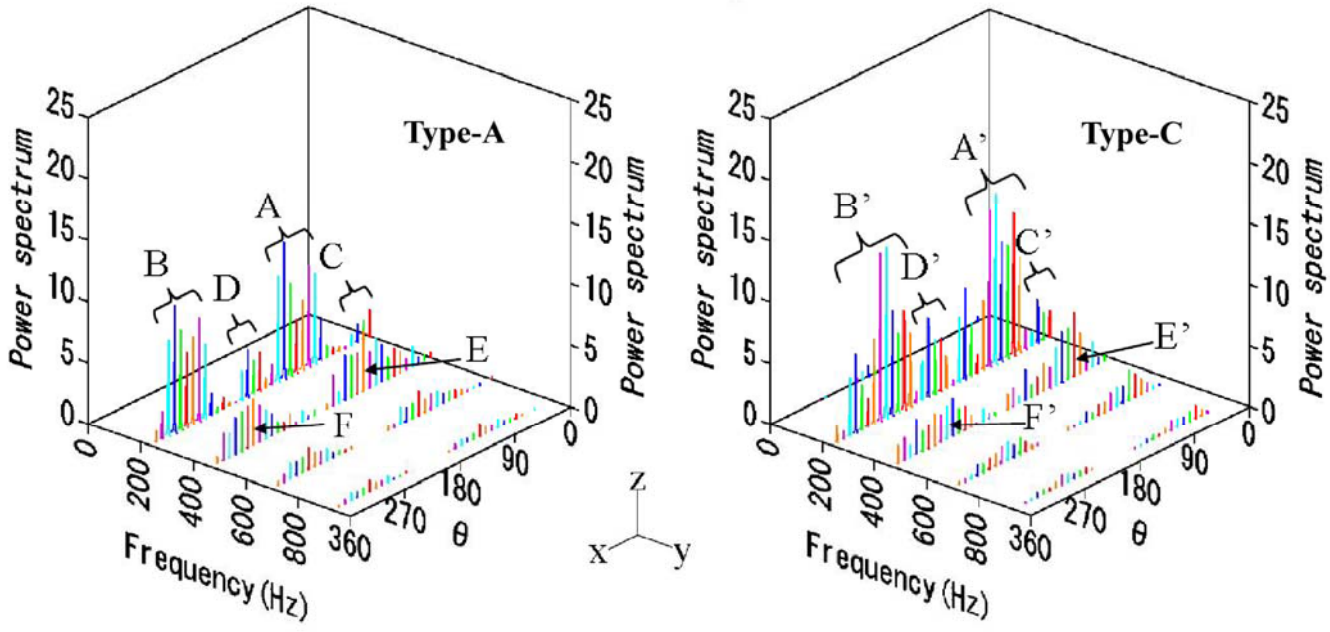


(a) Type-A (b) Type-C

**Fig. 9** Power spectral densities of the non-dimensional pressure on the outer perimeter

Figure 9 shows the power spectral density of the non-dimensional pressure along the outer perimeter at $\phi = 0.03$ for Type-A and Type-C. Note that there is no spectrum at 33Hz for either types, as this frequency corresponds to the rotation speed of impeller $n$ = 2000 rpm. A strong power spectrum is observed at 233 Hz, due the blades passing near the upper and lower tongues ($\theta = 0^\circ$ and $180^\circ$) in the regions A and B (Type-A), and the regions A' and B' (Type-C). In these regions, the flow patterns on the front and back of the blade are very different.

In regions C and D for Type-A, and C' and D' for Type-C, the spectrum at 233 Hz dominates and no overtone is observed at 467 Hz. However, this overtone is observed in regions E and F for Type-A, and E' and F' for Type-C, resulting from the pressure deviations from both the upper and lower tongues.

Concave curves are observed in regions of A, B, A', and B' at 233 Hz, at the same positions where the spectrum maxima appear in regions of E, F, E', and F' at 467 Hz. This indicates that some energy at 233 Hz is transferred to 467 Hz as a result of having an odd number of blades ($Z_I$ =7), which causes a decrease in the pressure deviation exerted on the blades.

## 6. **Pressure and flow in the volutes**

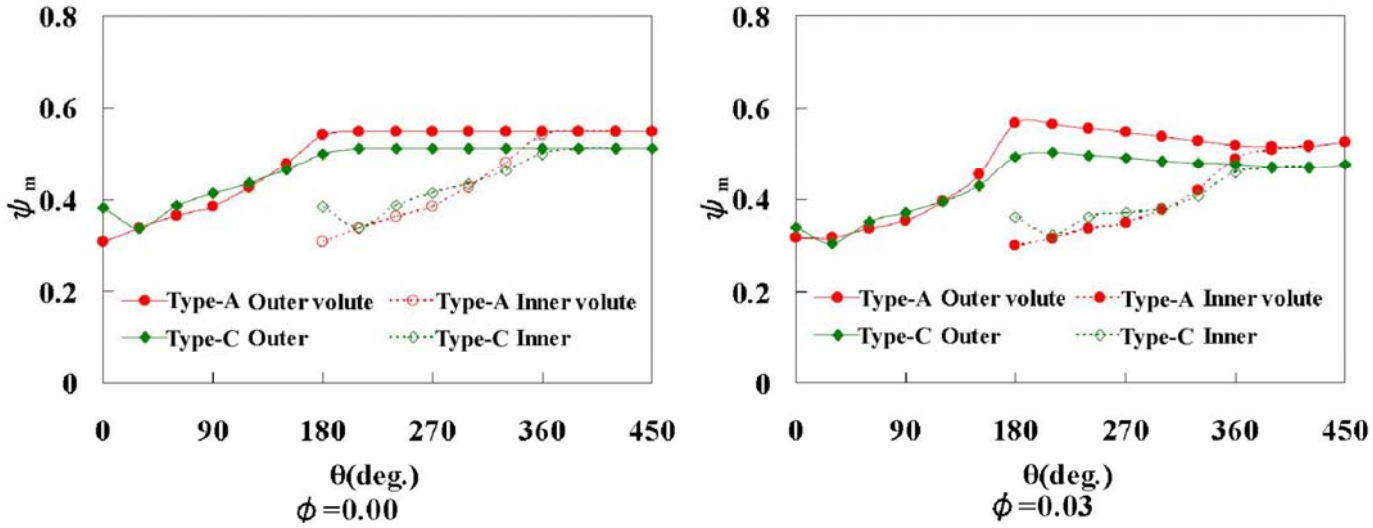


**Fig. 10** Averaged non-dimensional pressure in the volutes

Figure 10 shows the averaged non-dimensional pressures in the outer and inner volutes for $\phi = 0.00$ and 0.03, measured along the center of each volute channel at points separated by $30^\circ$. The junction of the two volutes is located at $420^\circ$ and the outlet at $450^\circ$.

For both flow rates and for both model types, the pressure in the regions $30^\circ$-$150^\circ$ for the outer volute and $210^\circ$-$330^\circ$ for the inner volute increases with the angle. The effect of the difference in the volute shape on the pressure appears in the regions $180^\circ$-$450^\circ$ for the outer volute and $360^\circ$-$450^\circ$ for the inner volute. In these regions, the pressure for Type-A is larger than for Type-C because the volute cross-sectional area in Type-A is smaller, and a higher pressure is required to overcome the higher fluid resistance. Further, the pressure at $\phi = 0.00$ is almost constant because the averaged flow rate is zero, whereas the pressure at $\phi = 0.03$ decreases with angle because the pressure gradient drives the fluid flow. Therefore, to obtain a higher pump head for our pump with the specifications mentioned previously, the design of the Type-A model is more suitable.

For $\phi = 0.00$, the pressure in the regions $0^\circ$-$180^\circ$ for the outer volute and $180^\circ$-$360^\circ$ for the inner volute are very similar because the channel near the outlet affects the pressure negligibly, due to the absence of flow in this area. For $\phi = 0.03$, the pressure in the region $270^\circ$-$360^\circ$ for the inner volute is slightly higher than in the region $90^\circ$-$180^\circ$ for the outer volute because the length of the outer volute between the upper tongue and the outlet is greater than that of the inner volute between the lower tongue and the outlet. This discrepancy results in a greater fluid resistance to overcome. For the same reason mentioned above, the non-dimensional pressure between $270^\circ$ and $360^\circ$ in Fig. 7 is slightly higher than between $90^\circ$ and $180^\circ$.

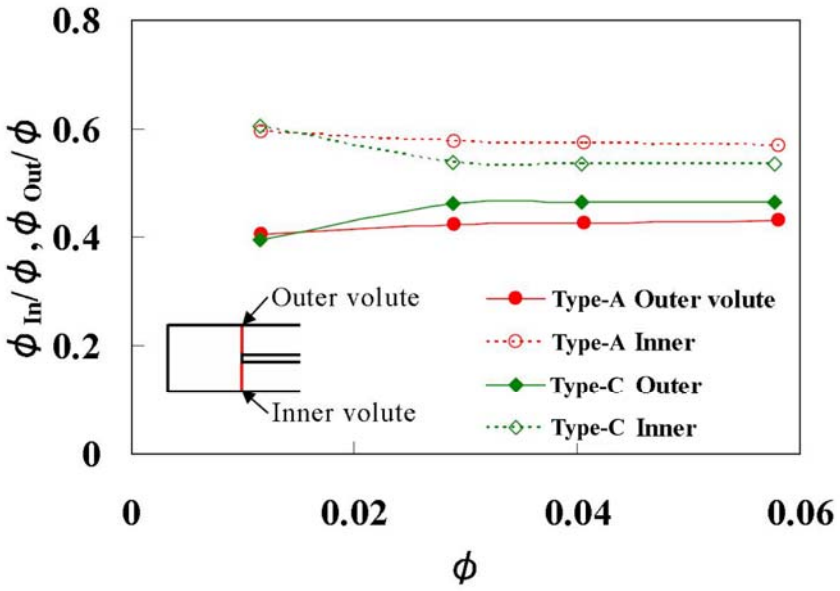


**Fig. 11** Flow rates in the outer and inner volutes

Figure 11 shows averaged flow rates in the outer ( $\phi_{out}$ ) and inner ( $\phi_{in}$ ) volutes, measured over the cross section at the junction denoted in the inset by a red line. These values are normalized by the total flow rate $\phi$ . The flow rates in the inner volute for both types are larger than those in the outer volute because of the shorter channel and smaller fluid resistance in the inner volute.

In Type-A, the difference in the outer and inner volute flow rates is almost independent of the total flow rate, whereas in Type-C the difference decreases as the total flow rate increases. This is because the cross-sectional areas of the volutes in Type-C are wider than in Type-A, so that the difference between the fluid resistances in the outer and inner volutes is much smaller.

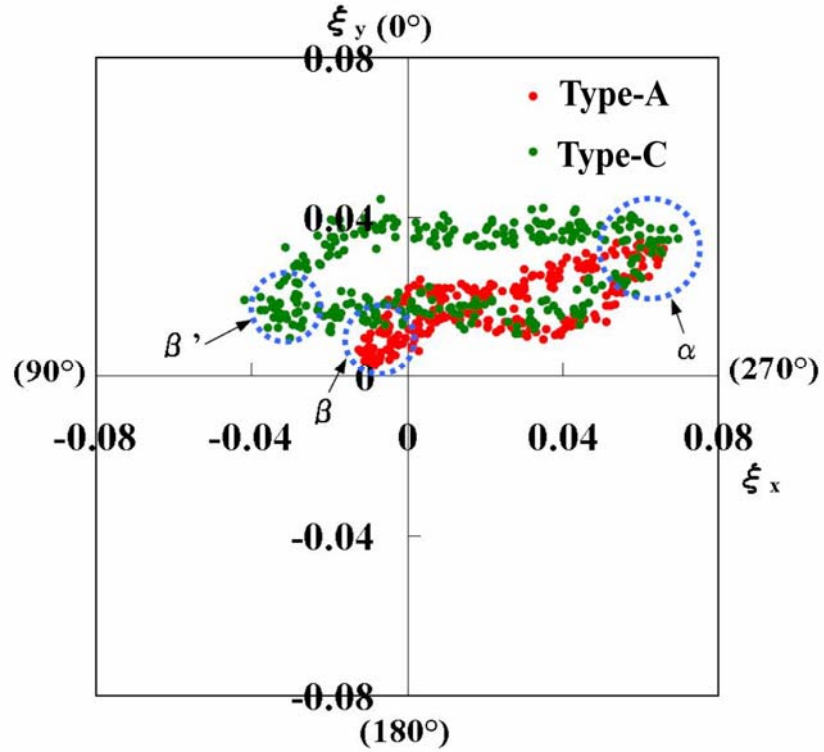


**Fig. 12** Unsteady fluid force on impeller

## 7. **Unsteady fluid force on impeller**

This section considers the unsteady fluid force that produces the vibratory movement of the impeller axis.

Figure 12 shows the $x$- and $y$-components of the non-dimensional fluid force, $\xi_x$ and $\xi_y$ , acting on the impeller in both model types, measured during one rotation at flow rate $\phi = 0.03$ . These forces are calculated by integrating the pressure and viscous force over the impeller blade surfaces. This Lissajous figure rotates clockwise, in the direction opposite to the impeller's rotation.

The green and red data points in region $\alpha$ are measured when a blade passes near the lower tongue, and those in regions $\beta$ and $\beta'$ when it passes near the upper tongue. The force in the $y$-direction is always positive, and that in the $x$-direction oscillates between positive and negative values for both model types. These fluctuating forces are seen as the main cause of the vibration of the impeller axis.

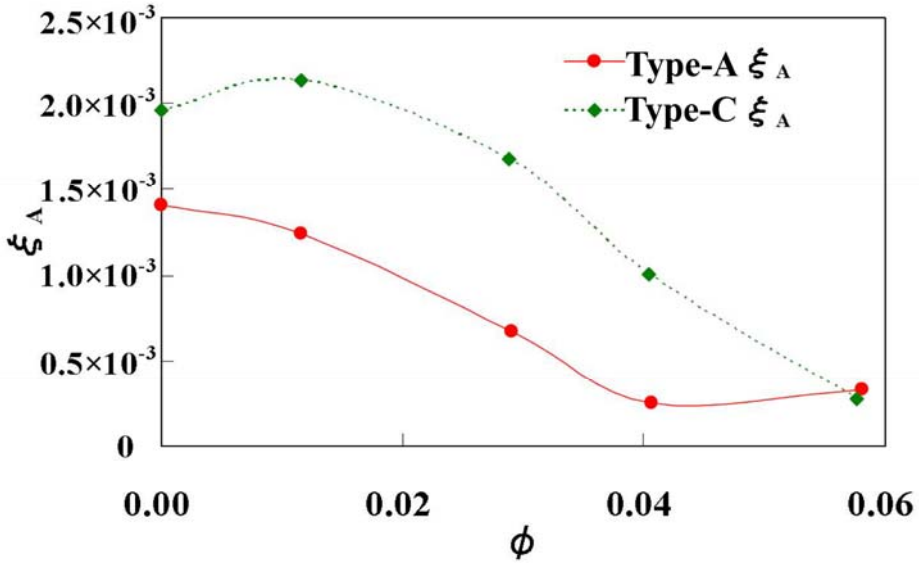


**Fig. 13** Area of Lissajous figure of fluid force components at various flow rates

To compare the fluctuation magnitude of the unsteady fluid force exerted on the impeller for different flow rates, the area of the Lissajous figure is plotted in Fig. 13. This area is larger for Type-C than for Type-A, suggesting that Type-C will give rise to larger impeller axis vibrations and require more energy to achieve stability. Moreover, the stability increases with increasing flow rate for the range of values considered here.

Figure 14 shows averaged $x$- and $y$-components of fluid force, $\xi_{mx}$ and $\xi_{my}$ that correspond to the center of gravity of the Lissajous figures in Fig.12. Figure 15 shows their standard deviations, $\xi_{sx}$ and $\xi_{sy}$.

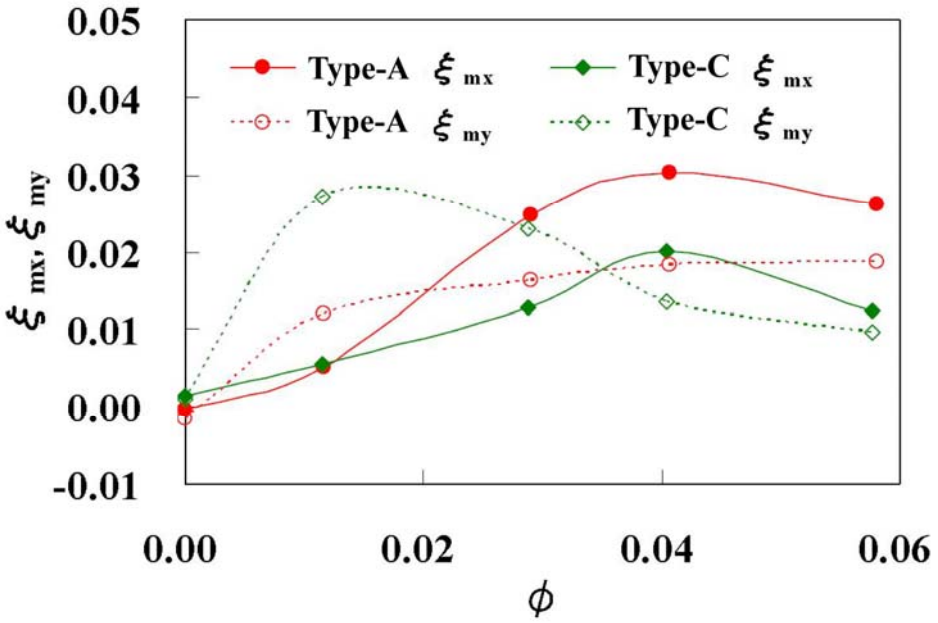


**Fig. 14** Averaged components of the fluid force

Figure 14 shows that the averaged values, $\xi_{mx}$ and $\xi_{my}$ depend on both the flow rate $\phi$ and the model type except at $\phi$ = 0.00. The averaged forces for both types are positive, consistent with the axis rotating in the direction of increasing $\theta$. This results from the averaged pressure in the range 90°-170° on the outer perimeter (Fig.7) and the pressure in the volute (Fig.10) being slightly greater than in the range 270°-360°.

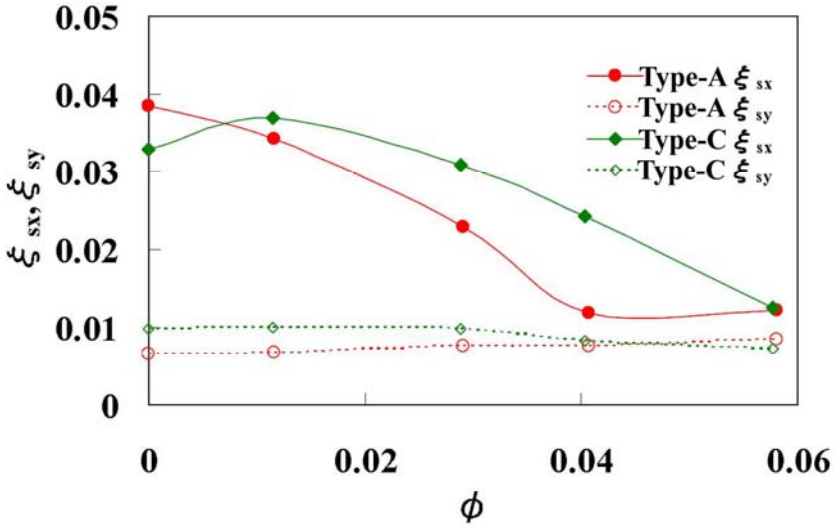


**Fig. 15** Standard deviation of components of the fluid force

Figure 15 indicates that the standard deviation of the averaged fluid force in $x$-direction, $\xi_{sx}$, for Type-A is larger than for Type-C except for $\phi = 0.00$. It decreases with $\phi$, and becomes almost identical for the two model types at $\phi = 0.06$. On the other hand, the standard deviation in $y$-direction, $\xi_{sy}$, remains almost constant at 0.01 for both types over the whole range of $\phi$. The stability should thus increase with the flow rate as mentioned above.

The area of the Lissajous figure of the fluid force, $\xi_A$, and the standard deviations, $\xi_{sx}$ and $\xi_{sy}$ for Type-A are generally smaller than for Type-C, suggesting smaller vibrations and a better impeller stability for Type-A than Type-C. For reasons of energetic efficiency and, at worst, to prevent the loss of control, the Type-A model with a narrower volute cross-sectional area is a better design for a blood pump than the Type-C model.

## 8. Conclusion

To study the vibration of the axis of impeller magnetically suspended in a blood pump, we conducted numerical simulations for two models with different volute cross-sectional areas using a computational fluid dynamics software. Because of the difficulty in simulating the impeller axis behavior at every time step, we simplified the analysis of unsteady pressures and fluid forces by assuming a fixed axis.

Our results lead to the following conclusions:

1. The pump of a volute with narrower cross-sectional area is suitable for patients who require a high blood pressure, whereas a wider cross-sectional area is more suitable for large patients who require a large blood flow rate.

2. Due to the design of double volute, the averaged pressure along the outer impeller perimeter is almost the same, and symmetrical with respect to the center of the impeller, regardless of the difference in the cross-sectional area of the volutes.

3. The pressure deviation on the impeller decreases by employing an odd number of blades for the double volute with the upper and lower tongues.

4. The fluid force exerted on the impeller varies with the flow rate and the shape of the volute, and it is presumed that the vibratory movement of the impeller is smaller for a volute with a narrower volute.

5. The fluctuation of the fluid force decreases with increasing flow rate.

## Acknowledgments

We would like to extend our gratitude to Teruaki Akamatsu, Professor Emeritus, Kyoto University, for his insightful suggestions throughout this study.

## Nomenclature

$b$ Height of blade [mm]

$F_j$ Components of fluid force [N]

$F_{sj}$ Standard deviation of fluid force components

$$F_{sj}=\sqrt{\frac{\sum_{i=1}^{n}\left(F_{ji}-\overline{F_j}\right)^2}{n-1}}$$

$n$ Rotation speed [ $min^{-1}$]

$P$ Pressure [mmHg]

$P_m$ Averaged pressure [mmHg]

$$P_m=\frac{\sum_{i=1}^{n}p_i}{n}$$

$P_s$ Standard deviation of pressure [mmHg]

$$P_s=\sqrt{\frac{\sum_{i=1}^{n}\left(p_i-\overline{p}\right)^2}{n-1}}$$

$Q$ Discharge rate [L/min]

$Q_I$ Discharge rate of impeller [L/min]

$Q_{In}$ Discharge rate at inner volute [L/min]

$Q_{Out}$ Discharge rate at outer volute [L/min]

$r_1$ Impeller inner radius [mm]

$r_2$ Impeller outer radius [mm]

$v_r$ Radial velocity [m/s]

$\xi_A$ Area of non-dimensional fluid force

$$\xi_A=\frac{1}{2}\left\{\sum_{i=0}^{n-1}(\xi_{xi}\xi_{yi+1}-\xi_{xi+1}\xi_{yi})\right\}$$

$\xi_j$ Non-dimensional fluid force

$$\xi_j=\frac{2F_j}{\rho\omega^2r_2^4}$$

$\xi_{mj}$ Non-dimensional averaged fluid force

$$\xi_{mj}=\frac{1}{6\xi_A}\left\{\sum_{i=0}^{n-1}(\xi_{ji}+\xi_{ji+1})(\xi_{xi}\xi_{yi+1}-\xi_{xi+1}\xi_{yi})\right\}$$

$\xi_{sj}$ Standard deviation of non-dimensional fluid force

$$\xi_{sj}=\frac{2F_{sj}}{\rho\omega^2r_2^4}$$

$\rho$ Density of blood [$kg/m^3$]

$\phi$ Non-dimensional flow rate at the outlet:

$$\phi=\frac{Q}{2\pi r_2^{\,2}b\omega}$$

$\phi_I$ Non-dimensional flow rate of impeller:

$$\phi_I=\frac{Q_I}{2\pi r_2^{\,2}b\omega}$$

$\phi_{In}$ Non-dimensional flow rate at inner volute

$$\phi_{In}=\frac{Q_{In}}{2\pi r_2^{\,2}b\omega}$$

$\phi_{Out}$ Non-dimensional flow rate at outer volute

$$\phi_{Out}=\frac{Q_{Out}}{2\pi r_2^{\,2}b\omega}$$

$\psi$ Non-dimensional pressure at outlet:

$$\psi=\frac{P}{\rho(r_2\omega)^2}$$

$\psi_m$ Non-dimensional averaged pressure

$$\psi_m=\frac{P_m}{\rho(r_2\omega)^2}$$

$\psi_s$ Standard deviation of non-dimensional pressure

$$\psi_s=\frac{P_s}{\rho(r_2\omega)^2}$$

$\omega$ Angular speed [rad/s]

## References


[1] Akamatsu, T., 2003, "Artificial heart – Turbo type blood pump for long term use," *Nippon Rinsho*, Vol. 61, No. 5, pp. 881-885.

[2] Akamatsu, T., 1994, "Centrifugal Blood Pump (in Japanese)," Turbomachinery, Vol. 22, No. 1, pp. 40-46.

[3] Akamatsu, T., 2001, "Study of the magnetically suspended centrifugal blood pump (in Japanese)," Turbomachinery, Vol. 29, No. 1, pp. 7-16.

[4] Akamatsu, T., et al., 1992, "Centrifugal Blood Pump with a Magnetically Suspended Impeller," Artificial Organs, Vol. 16, No. 3, pp. 305-308.

[5] Tsukiya, T. and Akamatsu, T., 1995, "Development of the Centrifugal Blood Pump with Magnetically Suspended Impeller (in Japanese)," Transactions of JSME, 61-591, B, pp. 3913-3920.

[6] Ogami, Y., Matsuoka, D., Horie, M., 2010, "Computational Study of Magnetically Suspended Centrifugal Blood Pump (The First Report: Main Flow and Gap Flow)," International Journal of Fluid Machinery and Systems, Vol. 3, No. 2, pp. 102-112.